Manuscript entitled „Application of holography and automated image processing for laboratory experiments on mass and fall speed of small cloud ice crystals" by M. Weitzel et al.

We would like to thank all reviewers for the useful comments and interesting suggestions which helped improve the manuscript. The reviewers' comments and questions are answered in the following.

Remark:
The reviewers' comments are written in bold font, our answers in standard font.

AUTHOR'S REPLIES TO REVIEWERS' COMMENTS

Authors' response to reviewer #1:

" […] First, the vast majority of the ice crystals take on the shape of the ice crystals that are nucleated at a temperature of -30 °C or below rather than the ambient temperatures of their later growth (-8 to -16 °C). This can readily be seen in Figures 2 and 4, and as noted on lines 237-238 "the majority of ice crystals (~68%) showed irregular crystal growth, and aggregates. […] At these temperatures and for the sizes considered (equivalent diameters between 15 and 145 microns) the crystals should be dominantly planar and dendritic, not the types observed, especially aggregates, which generally form at sizes above 200 microns, suggesting very high ice concentrations."

The homogeneous nucleation method was developed initially to confirm the feasibility of the chamber experiments. It is a simple approach that does not introduce pollution with aerosol particles into the chamber and provides a reliable source of nucleation of a substantial amount of crystals. That said, a smaller number of experiments using INP as nucleation source were conducted to form an understanding of the influence of the nucleation mechanism on the crystals' growth behavior. While no quantitative analysis on these observations was conducted, a similar fraction of crystals with irregular shapes were observed after heterogeneous nucleation induced by ice nuclei (Montmorillonite). This suggests that the observed crystal shapes are influenced by the thermodynamic conditions during particle growth within the chamber rather than by the conditions during initial freezing.
As the reviewer suggests in their comment, a more thorough analysis of the differences

between particle growth after homogeneous and heterogeneous nucleation in the chamber would be interesting, and can be subject of future work. However, we do not expect any influence of the freezing mode (i.e. homogeneous or heterogeneous) on the fall velocity of ice crystals of the same habit.
An elaboration on the uncertainties in the understanding of the growth processes within the chamber has been added to the discussion section of the article (Line 222 and the following).

Authors‘ response to reviewer #2:

“There are other ´experimental´ studies of velocity of small ice particles in chambers e.g. those cited in Westbrook paper you mention (which are quite old) but also the more recent work by Argentinian group […] It would be very useful to put you work in context against those other studies”

In their work, the Argentinian group Bürgesser et al. studied the fall behavior of hexagonal planar (Bürgesser & Castellano, 2017) and column crystals (Bürgesser et al. 2016) by determining and relating Best- and Reynolds numbers. We have compared our results to the results of the latter study in Section 4.3 and Figure 9. This comparison indicated that the parameterization of Bürgesser et al. predicts significantly higher Best numbers than our experimental results.
As our experiments did not include many hexagonal planar crystals, we were not able to accurately establish whether our observations agreed or disagreed with the findings in Bürgesser & Castellano (2017).

“It might also be cold enough to nucleate ice homogeneously from vapour if there is flow of warmer air past this rod?”

Because of the large number concentration of ice crystals homogenously nucleated from droplets present in the air flow, we expect the pathway of homogenous nucleation to be negligible in this setup. The copper rod is kept at this very low temperature only for a limited time before it is flushed with warmer air. During this limited time of cold finger activation, the droplet supply is not expected to be depleted, thus crystals nucleated from droplets are always present. Supersaturations high enough to trigger homogenous nucleation from water vapour are thus very unlikely to be reached due to the preferred pathway of diffusion of water vapour towards the preexisting crystals.

“You could be more specific here. Do the points [Fig. 3b] outside the grey line tell us about the accuracy of the velocity estimates?”

The uncertainty of the velocity measurements themselves is significantly smaller than the spread observed here. The spread is thus a result of a superposition of the residual turbulence in the chamber and the accuracy of the velocity estimates.

“Are you able to match mass and diameter estimates from the particles on the slide to the corresponding velocity measurements of the particles in the tube? Or are you characterizing the average mass of similar crystals at around the same time (and what random error does that introduce?)

The concept of matching individual velocity measurements to mass measurements was considered during design of the experimental setup. The final setup, however, only allows for the comparison of ensembles of mass measurements to ensembles of velocity measurements, as the focus of this study was to maximize the number of individual m(D) and v(D) data points. The connection between our findings for mass and velocity can only be made by comparing the distributions of particle masses and the distribution of fall velocities measured during the same experiment.

This fact has been reemphasized in the corresponding text section of the revised manuscript in Section 3.2, lines 177 and following.

It shall be noted that this response has been repeated for the answer to a comment given by reviewer #3.

“I think it would be very useful to estimate the Reynolds number of the particles somewhere. Then you can establish the extent to which we should expect to be in the Stokes regime, as a function of D” […]

The Reynolds number of the observed crystals ranged between 0.1 and 0.7 (see Fig. 9). The observed fall behavior is thus not clearly in the Stokes regime (where Re would be << 1), with turbulence showing a minor impact on the observed fall velocity. A note has been added in line 307 and the following in the revised manuscript.

“In the Stokes regime it is surely not possible for $D_{hyd} > D_{max}$, but D_{maj} is not equal to the maximum span I suppose (how does it relate?) and perhaps at D_{maj} = 100 microns are you moving out of the Stokes regime?”

The description of ice crystals with respect to their maximum span D_{max} was never intended in this context, and the text and figures have been adjusted accordingly to correctly always use D_{maj}.

D_{hyd} is calculated from Equation 9. The mass power law relation given in Section 4.2 is applied to parameterize m on the right side of the equation here, which introduces two sources of error. Firstly, the parameterization is determined for the area-equivalent diameter of the crystal contour, D_{ae}, but applied to the long axis of an ellipse fit around the particle contour D_{maj} and thus not applicable strictly without error in this context. Further, the mass parameterization is most strongly determined by ice particles with sizes around 60 µm and, as evident from Fig. 5, mostly overestimates the mass of crystals with D > 100 µm. This overestimation of m also leads to an overestimation of D_{hyd} for those larger crystals. We thus do not expect that $D_{hyd} > D_{maj}$ would be observed for any crystals in individual measurements, but rather an asymptotical approximation of the fit to $D_{hyd} = D_{maj}$.

The relationship between D_{hyd} and D_{maj} proposed in this work is thus expected to accurately describe crystals with $D_{maj} < 90$ µm. For larger crystal sizes, more data would be required to either determine a new parameterization or adjust the one given here to be more accurate for all D_{maj}.

"Meaning is not clear – what is correlated with what, and how?" *(Re: Line 261 in the original draft, "Crystal habit and size show good correlation, as most crystals with $D_{maj} < 70$ µm have grown with a columnar or irregular habit, […]")*

We observed that none or very few of the observed columnar or irregular crystals grew to sizes $D_{maj} > 80$ µm. Most of the observed crystals between 80 and 200 µm were of dendritic shape or aggregates crystals, which is why we concluded a correlation between crystal size and habit in our observations. The text section in line 287 has been adjusted to be clearer.

"Re-X relationships: the authors could go a lot further in analysing the accuracy of parameterisations/theories, e.g. Mitchell 1996, Böhm 1989/1992, and Heymsfield and Westbrook 2010. You seem to have all the data to do this. Why not?"

We focused on the development and description of a new measurement technique for determining the properties of ice crystals in the size range smaller than 150 µm. While comparisons to related studies are important for understanding the context of this work's results, and have thus been conducted and described in Section 4, further analysis of the accuracy of other parameterizations is beyond the scope of this paper.

"I think the paper would greatly benefit from (i) more consistent use of characteristic length scale throughout, (ii) more explanation in the text of the rationale for picking a particular D for a given analysis or plot."

We incorrectly mentioned the particle maximum diameter D_{max} as the considered characteristic length scale in Figure 7 and the following text. These errors have been corrected, as D_{maj} is used for every aspect of this work where the results from holographic particle tracking are discussed.

To further clarify the usage of different characteristic length scales, Section 3.3 has been expanded to explain more clearly which formulation is used where and why.

"Consider providing data as a table / text file, as supplementary material?

We chose not to directly attach our data to this publication, as the data set is too large for convenient viewing. A publication on a suitable platform is planned at a future date. Nevertheless, all requests for our experimental data are very welcome and we are going to provide them for further scientific use.

Authors' response to reviewer #3:

"Line 85: Were particles measured in the fall chamber individually matched to the particles collected on the glass slides? It was not clear if the experiment supported this"

Reviewer #2 highlighted a similar point, and the same explanation given to them is appropriate here.

The concept of matching individual velocity measurements to mass measurements was considered during design of the experimental setup. The final setup, however, only allows for the comparison of ensembles of mass measurements to ensembles velocity measurements, as the focus of this study was to maximize the number of individual m(D) and v(D) data points. The connection between our findings for mass and velocity can only be made by comparing the distributions of particle masses and the distribution of fall velocities measured during the same experiment.

This fact has been reemphasized in the corresponding text section of the revised manuscript in Section 3.2, lines 180 and following.

Line 100: What is the estimated positional accuracy in all three directions for particles in the hologram?

The estimated positional uncertainty is $\Delta x = \Delta y = 9$ µm, and $\Delta z = 200$ µm along the optical axis. Since the fall velocity is calculated as the vertical component of the particles' motion, only Δy matters for the uncertainty in w. The resulting velocity uncertainty of $\Delta w_{track} = 0.5$ mm s^{-1} is considered along with the error introduced by residual turbulence (see Section 3.1.4), and a text section has been added in line 111 and the following to elaborate on this aspect.

Line 132: How many particles are in a typical hologram? Was the ice concentration so high that linking particles from one frame to another is difficult?

The most populated holograms contained up to several hundred crystals, which made linking challenging. The median particle number, however, was around 20. For these typical holograms, the third dimension made linking mostly easy.

Line 180: Were the same edge detection methods used for the holographic images as for the slide-captured images?

The detection method for hologram analysis involved a thresholding algorithm in the reconstructed slices. As many two-dimensional slices are reconstructed for each hologram, the signal created by the crystals are visible in several layers along the optical axis. This three-dimensional nature of the detected signal makes particle detection and noise filtering easier than in the case of classical two-dimensional imaging.

In the 2D case of microscope image analysis, thresholding often introduces errors created by incomplete edges or incorrect merging of multiple objects. To improve measurement accuracy, the more sophisticated segmentation methods described in Section 3.2 and the Supplement were implemented and compared.

Line 242 and Figure 5: Were the other power law relationships converted to use a consistent size definition (D_{eq} or D_{sec})? This can sometimes make a large difference.

We agree that the size definition has to be taken into account when applying power law relationships to determine the unknown mass of an ice particle from its size. The definition used plays a major role regarding the applicability and accuracy of parameterizations like the ones determined in this work. The parameterizations depicted in Figure 5 are shown without prior conversion however, as either additional information about the particles at hand or simplifying assumptions would have been required for an accurate conversion in several cases.

Line 243: What are the power law coefficients from this study (a and b), for both D_{eq} and D_{sec}?

D_{sec}: a = 0.03097, b = 2.13
D_{ae}: a = 0.4972, b = 2.36

The power law relationships including their parameters were added in Section 4.2, line 257 and the following.

Line 245: It is mentioned in the abstract that the other power laws were generally developed on larger particles and have been extrapolated down to the sizes in this study. I think this point needs to be reemphasized here.

A remark has been added in line 279 which reemphasizes that the power law relationships from the literature were determined from measurements of larger ice crystals.

Some discussion behind the observed differences would also be valuable, such as the types of particles (habit, degree of riming, etc.) that were collected in the other studies.

Section 4.2 has been expanded by more detailed descriptions of the origins of the parameterizations shown in Figure 5.

Also, is there a functional form that could bridge the gap between various small/large mass-size parameterizations?

We have not looked into determining a functional form to bridge the gap between several parameterizations. A future review article with the objective of finding such a relationship would be a valuable resource for handling the challenges of parameterizing particle mass.

Line 255: Related to the first comment, is the mass of each particle known, i.e. were the velocity measurements (either by hologram or fallstreak) directly linked to the mass measurement for each individual particle? If not, is m estimated from the power law in Section 4.2 to get D_{hyd}?

This question is mostly answered in our response on the first comment by the reviewer.

m is indeed parameterized from the power law obtained in Section 4.2 for the calculation of D_{hyd}. The errors introduced thereby are discussed in line 298 and the following.

Line 260: What is happening physically when D_{hyd} > D_{max}, and do you have any speculations or measurements to indicate why that transition occurs around 100um?

Again, Reviewer #2 asked a similar question, and the explanation given to them is repeated here.

D_{hyd} is calculated from Equation 9. The power law relation given in Section 4.2 is applied to parameterize m on the right side of the equation here, which introduces two sources of error. Firstly, the parameterization is determined for the area-equivalent diameter of the crystal contour, D_{ae}, but applied to the long axis of an ellipse fit around the particle contour D_{maj} and is thus not applicable strictly without erroring this context. Further, the mass parameterization is most strongly determined by ice particles with sizes around 60 µm and, as evident from Fig. 5, mostly overestimates the mass of crystals with D > 100 µm. This overestimation of m also leads to an overestimation of D_{hyd} for those larger crystals. We do not expect that $D_{hyd} > D_{maj}$ would be observed for any crystals in individual measurements, but rather an asymptotical approximation of the fit to $D_{hyd} = D_{maj}$.

The parameterization between D_{hyd} and D_{maj} proposed in this work is thus expected to accurately describe crystals with $D_{maj} < 90$ µm. For larger crystal sizes, more data would be required to either determine a new parameterization or adjust the one given here to be more accurate for all D_{maj}.

The discussion section has been extended in line 297 and the following by a paragraph explaining these considerations.

Line 278: The 3-D holographic track information is highlighted in the abstract and in a few places in the body of the manuscript, but I don't see any data on the lateral movement of the particles presented in this manuscript. Is there significant lateral movement of the particles? Were any tumbling motions observed? I think it would be valuable to add a figure or two to highlight any lateral movement (or lack thereof).

The observed lateral distances covered by the falling particles on their short way through the sample volume was mostly small when compared to the vertical movement. A sample figure showing the three-dimensional track of a falling particle along with the evolution of its measured properties has been added to Section S6 in the supplement. The ratio between lateral and vertical movement of the majority of all sampled crystals is in a similar range.

Line 295: Was there any attempt to measure the size of the particles in the fallstreak analysis, and how does the distribution compare with the holographic method?

The size of particles sampled in the fall streak method was not investigated directly from the streak images. The method was designed with the objective of optimizing the accuracy and quantity of the velocity measurements, which resulted in large errors if particle size were extracted from the width of the streaks. Size and velocity observed in this method can thus only be related through the distribution of the fall velocity (determined from streaks) and size (determined from microscopy afterwards) of ensembles of many crystals.

Manuscript entitled „Application of holography and automated image processing for laboratory experiments on mass and fall speed of small cloud ice crystals" by M. Weitzel et al.

List of changes in the revised manuscript

- **Section 3.1.1, Line 107 and following:**
  - Estimation of uncertainty in particle position added.

- **Section 3.1.2, Line 136 and 137:**
  - A reference to a visualization of the information gained from a sample particle track in the Supplement was added.

- **Section 3.2, Line 180 and following:**
  - Added a paragraph explaining that and why no direct matching between mass and velocity points is possible.

- **Section 3.3, Line 214 and following:**
  - Added further elaboration about the reasoning of used characteristic length scales.

- **Section 4, Line 226 and following:**
  - Added a paragraph discussing the influence of the cold finger nucleation method on the observed ice crystal properties.

- **Section 4.2, Line 261 and following:**
  - Added parameters a and b for the m(D) power law relation.

- **Section 4.2, Line 266 and following:**
  - Added a paragraph discussing the properties of ice crystals investigated in the studies from which m(D) parameterizations are shown in Fig. 5. The sample methods are described, along with the types of crystals, degrees of riming (if applicable) and the characteristic length scale used.

- **Section 4.2, Line 279 and 280:**
  - Added a remark underlining that, except for Mitchell 2010, all studies focused on investigating ice crystals larger than 100 µm

- **Section 4.3 and Figure 7:**
  - Changed incorrectly used characteristic size D_{max} to D_{maj} in several occurrences in the text, figure and caption.

- **Section 4.3, Line 290 and following:**
  - Adjusted this section for clarification.

- **Section 4.3, Line 296 and following:**
  - Added a paragraph explaining the occurrence of data points with $D_{hyd} > D_{maj}$ in Fig. 7 and error estimation. Added a remark limiting the applicability of the obtained D_{hyd} (D_{maj}) relationship to $D_{maj} < 90$ µm.

- **Section 4.3, Line 309 and 310:**
  - Added a comment about the applicability of the Stokes approximation.

- **Supplement:**
  - Added Section S6 with sample images of a typical holographic particle tracking observation and a fall streak recording

Application of holography and automated image processing for laboratory experiments on mass and fall speed of small cloud ice crystals

Maximilian Weitzel[1], Subir K. Mitra[1], Miklós Szakáll[2], Jacob P. Fugal[2,3], and Stephan Borrmann[1,2]

[1]Max Planck Institute for Chemistry, Mainz, Germany
[2]Institute of Atmospheric Physics, University of Mainz, Mainz, Germany
[3]Now at SeeReal Technologies

Correspondence: Miklós Szakáll (szakall@uni-mainz.de)

Abstract. An ice cloud chamber was developed at the Johannes Gutenberg University of Mainz for generating several thousand data points for mass and sedimentation velocity measurements of ice crystals with sizes less than 150 µm. Ice nucleation was initiated from a cloud of supercooled droplets by local cooling using a liquid nitrogen cold finger. Three-dimensional tracks of ice crystals falling through the slightly supersaturated environment were obtained from the reconstruction of sequential holographic images, automated detection of the crystals in the hologram reconstructions, and particle tracking. Through collection of the crystals and investigation under a microscope before and after melting, crystal mass was determined as a function of size. The experimentally obtained mass versus diameter ($m(D)$) power law relationship resulted in lower masses for small ice crystals than from commonly adopted parameterizations. Thus, they did not support the currently accepted extrapolation of relationships measured for larger crystal sizes. The relationship between Best (X) and Reynolds (Re) numbers for columnar crystals was found to be $X = 15.3Re^{1.2}$, which is in general agreement with literature parameterizations.

1 Introduction

While the size distributions and number concentrations of ice crystals prevalent in different types of clouds throughout the atmosphere are extensively investigated by airborne in-situ measurements and various remote sensing techniques, knowledge of other microphysical properties of these ice particles remains much more elusive (Baumgardner et al., 2017). Thus, the properties of interest are often parameterized to allow the description of important processes like radiative transfer or the evolution of clouds over time in weather and climate models. The ice water content (IWC) in clouds for example has been the subject of several studies but is often difficult to determine accurately. Alternatively, if combined knowledge of the size distribution of ice particles in a cloud and the mass of each individual crystal is available, the IWC can be inferred indirectly. Cotton et al. (2013) described the ice particle mass using an effective density ρ_{eff}, defined as the mass of the particle m divided by the volume of a sphere with diameter equal to the particle's maximum diameter D_{max}. Thus, a crystal's mass is given as

$$m(D) = \frac{\pi}{6}\rho_{eff} D_{max}^3. \quad (1)$$

ρ_{eff} is evidently lower than the density of bulk ice, as it accounts for the complex non-spherical shapes of pristine single crystals and aggregates, as well as inclusions of air inside the crystals in the form of small voids or bubbles. Locatelli and Hobbs (1974) and Mitchell et al. (1990), among others, studied ρ_{eff} through ground-based collection of ice crystals, focusing on the direct analysis of individual crystals. Other studies (e.g. Heymsfield et al. (2010), Cotton et al. (2013)) made use of aircraft-based in-situ observations, deriving relationships between particle size distributions measured by optical array probes and the IWC determined using other instruments. An alternative description of crystal mass can be given by expressions of the generalized form $m(D) = aD^b$, where a and b are empirically derived parameters and D is a representation of the crystal's dimension. With such a relationship, a dependency of ρ_{eff} on particle size is implied, an assumption that is also supported by theoretical work (Westbrook, 2007).

Another unresolved key parameter in cloud microphysics is the sedimentation velocity of ice crystals of sizes below 150 µm. Understanding the transport of mass and particle numbers within clouds is essential for accurately modeling many atmospheric processes, such as the formation of precipitation (Heymsfield et al., 2007) and transport and vertical redistribution processes such as denitrification (Molleker et al., 2014). Generally, the terminal velocity of a falling particle is attained if the gravitational force F_g is equal to the drag force F_D acting on the particle. The drag force experienced by a falling particle can be expressed using a dimensionless drag coefficient C_d as follows:

$$F_d = \frac{1}{2}\rho_a v^2 A C_d, \tag{2}$$

with a crystal falling through air with density ρ_a with velocity v while the area of the crystal projected normal to the fall motion is A. When equating Eq. (2) with the gravitational force $F_g = mg$, one obtains an expression for the sedimentation velocity as

$$v = \sqrt{\left(\frac{2mg}{\rho_a A C_d}\right)}. \tag{3}$$

In addition to A, the fall velocity evidently also depends (amongst others) on the mass m of the crystal, as well as C_d. The latter is a function of the Reynolds number Re, which represents the ratio between inertial and viscous forces that govern a particle's motion through the air and can be written as

$$Re = \frac{\rho_a v D}{\eta}, \tag{4}$$

where η is the dynamic viscosity of air. The Best number X (Davies, 1945) has been frequently used to elegantly describe fall velocity as a function of the other relevant properties (m, A, D). It is defined as:

$$X = C_d Re^2 = \frac{\rho_a}{\eta^2}\frac{2mgD^2}{A}. \tag{5}$$

As X itself is independent of the fall velocity v, relating it to the Reynolds number (which is a function of v, but independent of all other particle properties) yields a representative estimation for the particle sedimentation velocity from m, D and A (Heymsfield et al., 2010; Mitchell, 1996). This approach proves useful if all of these properties are known or characterizable through approximations and parameterizations.

A different approach for this problem, which was initially described by Hubbard and Douglas (1993), has been adapted by Westbrook (2007). It involves calculating the fall velocity of crystals from the Stokes solution for a falling object with the hydrodynamic radius R_{hyd}. While $R_{hyd} = R$ for spherical objects, a suitable description that accounts for the different flow characteristics around the falling object is required for other crystal shapes. If R_{hyd} is known, the fall velocity v can be calculated as

$$v = \frac{g}{6\pi\eta}\frac{m}{R_{hyd}}, \tag{6}$$

which is valid for small Reynolds numbers ($Re \ll 1$, i.e. $R_{hyd} \lessapprox 10\,\mu\text{m}$) where the flow is dominated by viscous forces.

For both mass and fall velocity, the amount of usable data in the literature is particularly sparse for ice crystal sizes smaller than $150\,\mu\text{m}$. Currently used parameterizations are often extrapolated from measurements of particles with significantly larger sizes and assumed to also be valid for those small particles. For ice crystal mass in particular, some studies assumed crystals smaller than a certain threshold to have the same mass as a spherical object with the density of bulk ice. Hence, the present study focuses on decreasing the uncertainties in the characterizations of ice crystals in the size range smaller than $150\,\mu\text{m}$ by creating a data set containing the properties of several thousand small ice particles. For this, automated object detection techniques were developed and applied to images and holograms recorded by an experimental setup designed specifically for the purpose of investigating small cloud ice particles. In Sect. 2, the ice cloud chamber that was used for the generation and analysis of the particles in a laboratory is described. Sect. 3 contains a description of the instrumentation and methods utilized for the determination of ice crystal mass and fall velocity. The results obtained from the conducted experiments are discussed in Sect. 4, and a summary and conclusion follow in Sect. 5.

2 Ice cloud chamber

An ice cloud chamber (ICC) was developed for the measurement of ice crystal sedimentation velocity through particle tracking in a three-dimensional volume, supplemented with the determination of particle mass through microscopic analysis of their melting product. In the ICC (Fig. 1), which was placed in the walk-in cold room of the Mainz vertical wind tunnel laboratory, locally-produced ice crystals in the size range smaller than $150\,\mu\text{m}$ can be investigated. The main part of the ICC is constructed inside the cold room and has a cylindrical shape spanning $3\,\text{m}$ in height and $60\,\text{cm}$ in diameter. Air circulation is induced by a fan in a secondary channel connecting the bottom of the chamber to the top (Label 2 in Fig. 1). In order to create a cloud in the chamber volume, this circulation is supplied with droplets generated by an ultrasonic nebulizer (Label 1 in Fig. 1). Once a sufficiently stable cloud has formed, the circulation is stopped, and ice particle nucleation is triggered at the top of the chamber. A hollow copper rod protruding into the chamber (Label 3 in Fig. 1) is filled with liquid nitrogen, inducing temperatures below 195 K, hence cold enough to trigger homogeneous freezing of the present droplets in the immediate vicinity of the rod. The newly formed crystals grow in the supersaturated environment maintained by the evaporation of liquid droplets while sedimenting towards the bottom of the chamber.

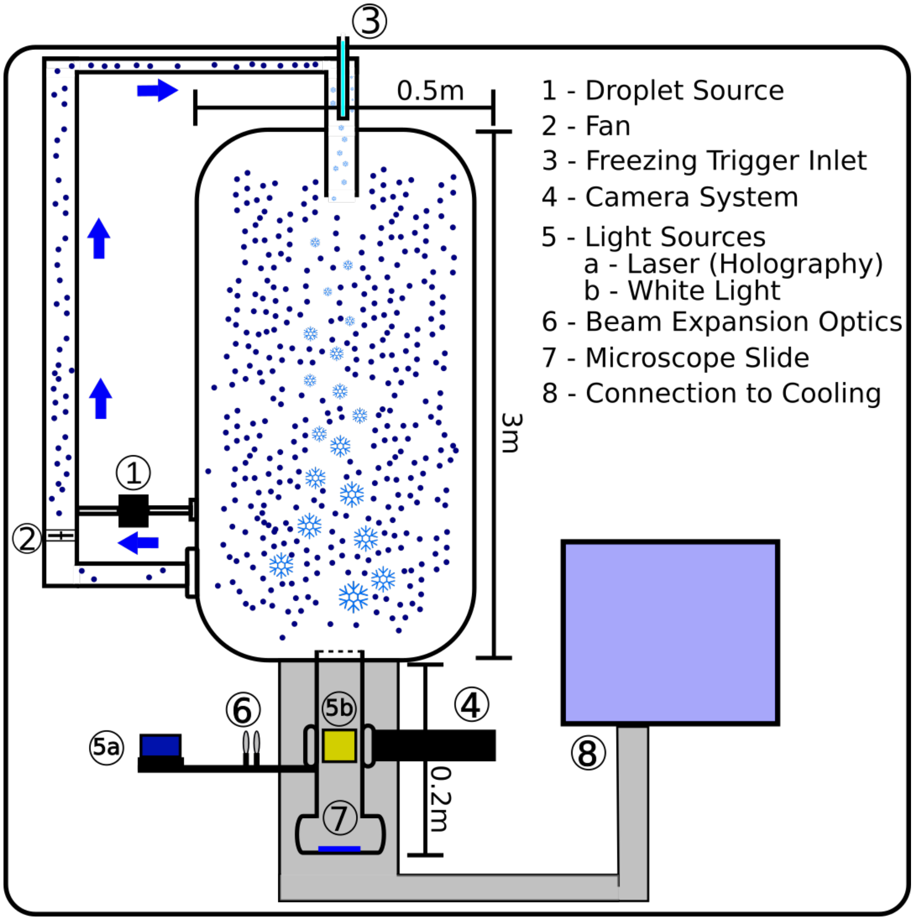

Figure 1. Schematic (not to scale) of the ICC from a side view. Droplets are generated and introduced into the chamber from an ultrasonic nebulizer (1) and mixed throughout the chamber through circulation created by a fan (2). After the desired cloud conditions are reached, freezing can be triggered in the top region using a cold finger (3). The measurement section (4-7), where mass and fall velocity measurements are conducted, is suspended below the chamber and ventilated with air from a cooling unit (8) to improve static stability.

The measurement section is mounted to the lowest part of the chamber and connected through an outlet. Particle fall velocity was measured by means of an in-house developed holographic instrument (see Sect. 3.1) which is positioned in a way that aligns its optical path through two windows in both of the side walls of the measurement section. A collector containing a microscope slide positioned in the center of a lid closed off the measurement section at the bottom. This collector was employed to catch the falling crystals for subsequent analysis using a digital camera mounted on a microscope.

3 Methodology

3.1 Sedimentation velocity

Figure 2 shows the in-house developed "Holographic Imaging and Velocimetry Instrument for Small Cloud Ice" (HIVIS) used for particle tracking in a sketch **(a)** and a photograph taken from the side **(b)**. HIVIS is an implementation of the classic optical setup for in-line holography (Silverman et al., 1964; Borrmann et al., 1993; Raupach et al., 2006) as applied to in-situ cloud

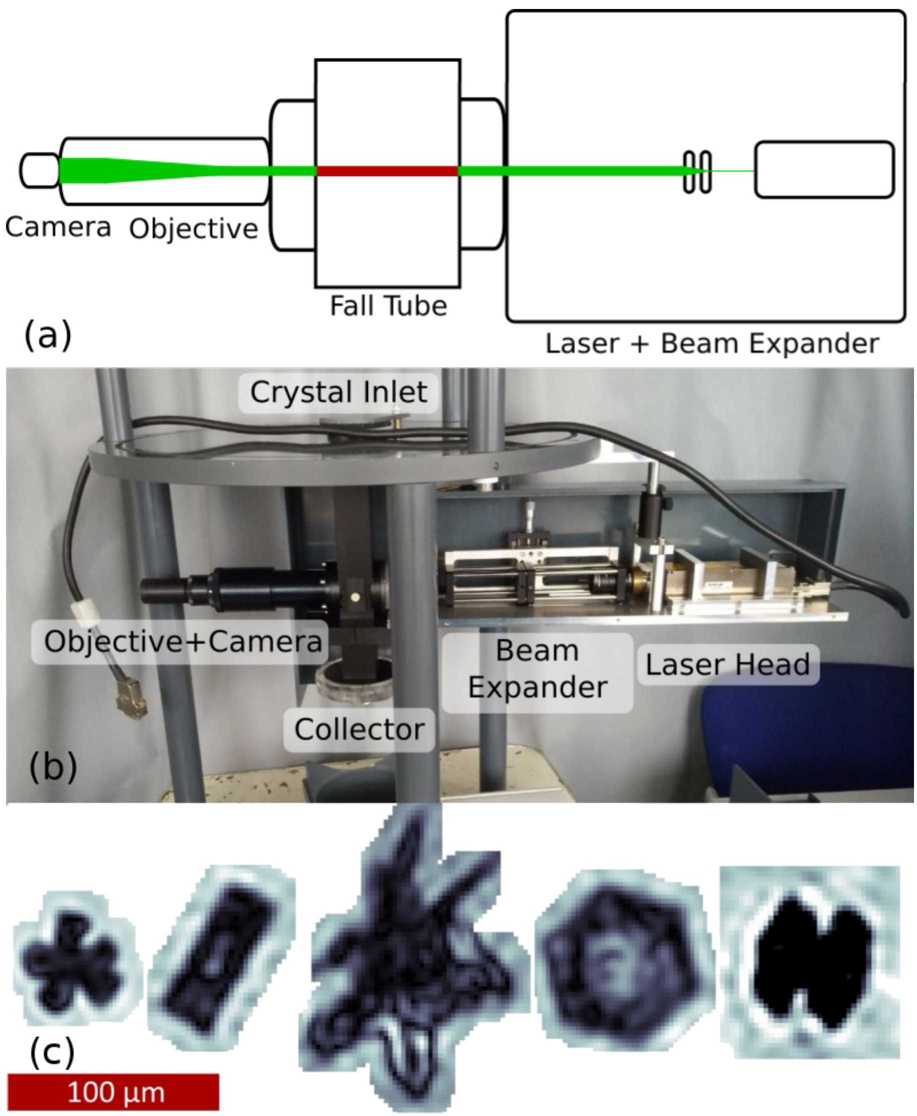

Figure 2. The HIVIS instrument used for holographic imaging. **(a):** Sketch of top-down view (sample volume in red), **(b):** photograph taken from the side. **(c)**: sample reconstructed images of ice crystals recorded by the HIVIS instrument.

measurements. The instrument's camera sensor is illuminated by an expanded and collimated beam emitted by a Nd:YAG laser with a wavelength of 532 nm. The hologram plane created and utilized by this setup has an area of $A_{sample} = 6.2 \times 4.9$ mm^2. Combined with the reconstruction depth of 4 mm, this leads to a sample volume of 4.86 cm^3. The crystals falling through this sample volume create scattered waves which interfere with the remaining undisturbed part of the laser beam (reference wave). The interference pattern (the hologram) is recorded by the camera, hence allowing the numerical reconstruction of an in-focus image of the original particle (Fugal et al., 2004). The camera records about 53 frames per second, yielding at least 3 and up to 10 recordings of crystals during their passage through the sample volume where they fall with a typical velocity of 20 to 100 mm/s.

3.1.1 Object detection

To prepare for the extraction of data from the recorded holograms, most of the background pattern and speckle noise created by dirt on the optical surfaces between camera and laser were removed during preprocessing and reconstruction (Fugal et al., 2009; Schlenczek, 2018). For this, a software filter was applied that divides every pixel's intensity in the hologram recorded at time $t = t_0$ by a value that represents the median of intensities $\bar{I}_{slice} = \frac{1}{N}\sum_{n=-N/2}^{N/2} I(t_0 + n)$ of this pixel in a set of holograms recorded shortly before and after t_0. The reconstruction for each hologram was then calculated following the convolution method described in Fugal et al. (2004), resulting in a stack of 2D images with a spatial resolution of $dz = 100$ µm (with z representing the spatial axis along the optical path of the laser) throughout the measurement section for each hologram. An object detection algorithm was applied which determined the position of the detected objects in three dimensions and their in-focus images through analysis of several image parameters deduced from both the intensity and phase reconstructions (see Sect. 5 in Fugal et al. (2009)). The uncertainty in the position determination with this method was estimated as $\Delta z =$ 200 µm in the direction along the optical axis and $\Delta x = \Delta y =$ 9 µm in the other lateral and the vertical direction.

A classification model based on decision trees was created and applied to filter out speckle noise from detections of actual particles and to separate among different crystal habits. First, a training data set was generated by the operator classifying a set of several hundred crystal images into one of the following different categories: artifact (disturbance in the reconstructed image generated by noise), irregular, dendritic, columnar and plate-like. Next, different particle properties were calculated from the intensity and phase images of each detected object. These properties included simple shape parameters (e.g. axis lengths of enclosing ellipse, total particle area), derived context information about amplitude and phase, and spatial position (e.g. distance to image center) to account for image inhomogeneity. From this set of classification data, a decision tree was created algorithmically in a way that splits the source set of classified objects into different subsets using a binary splitting criterion that optimizes the split at each node (Breiman et al., 2017). This was done to infer the class membership of the entire data set from the training subset and the corresponding binarization patterns. The parameters of each object were investigated following the tree from top to bottom, leading to an unambiguous path which lead to an endpoint representing a class. For validation purposes, the automated classifier that was generated using this method was applied to a test set of detections and compared to labels created by the operator, yielding an agreement of over 85%.

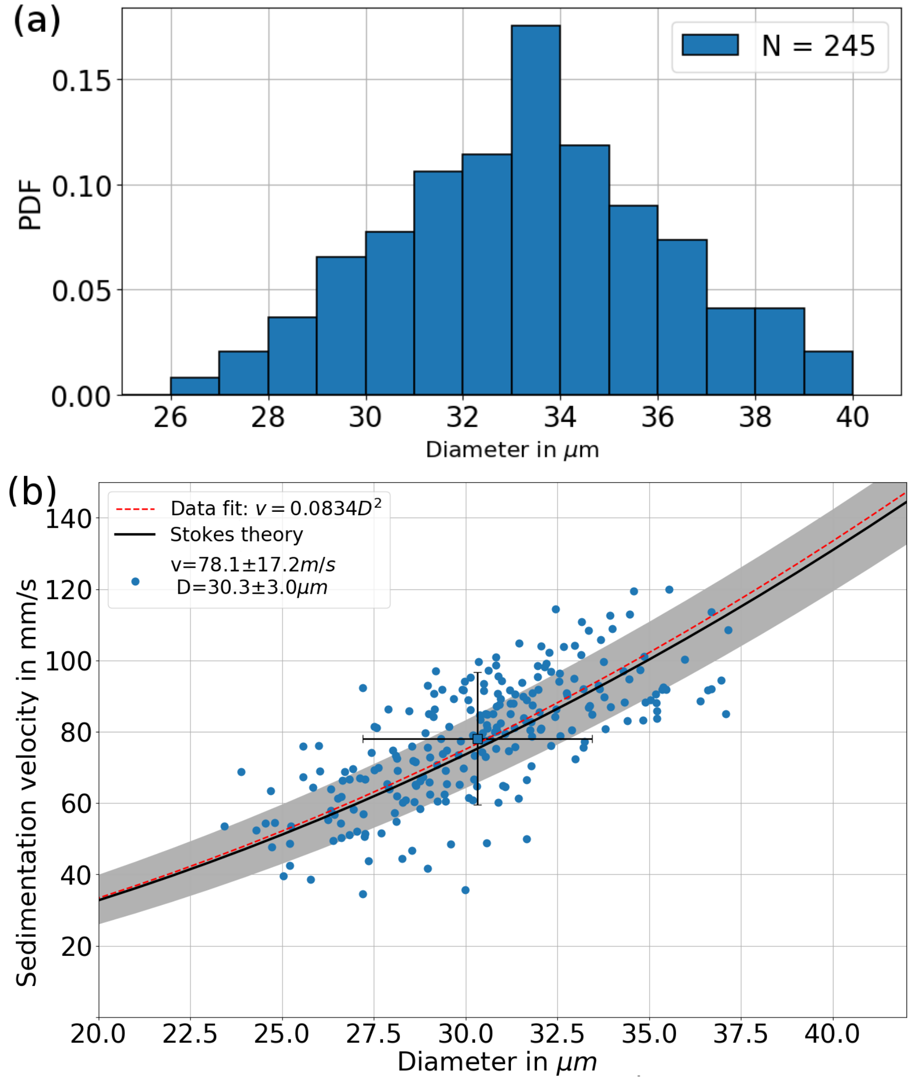

Figure 3. (a): Distribution of measured calibration sphere diameters before size corrections. **(b)**: Fall velocity as a function of (size-corrected) calibration sphere diameter for single calibration measurement fall tracks, quadratic fit as red dashed curve. The black curve shows the velocity expected from Stokes' law as a function of glass sphere diameter for $\rho_g = 2500$ kg m^{-3} with uncertainty as gray shading. The black marker shows mean and standard deviations of the measurement data.

3.1.2 Particle tracking

The sedimentation velocity of the falling particles has been determined by tracking their position throughout the three-dimensional sample volume (in the vicinity of the area labeled "5b" in Fig. 1). For each ice crystal object with size D that was detected in the hologram at $t = t_0$, a position $\boldsymbol{x}_{pred}$ in the hologram at $t_1 = t_0 + \Delta t$ is predicted using an estimated fall velocity v_{est} calculated from the Stokes solution for a sphere with diameter D, following

$$v = \frac{g}{3\pi\eta}\frac{m}{D}, \tag{7}$$

with η being the dynamic viscosity of air and m the crystal mass. If a crystal with similar properties (habit and size) was found close to this predicted position, the actual velocity was calculated from the particle's actual position at t_1 and the time step Δt. Using a leniency distance L, crystals are accepted as part of the fall track if their position x_1 lies within the region in space defined by $|\boldsymbol{x}_{pred} - \boldsymbol{x}_1| \leq L$. Crystals were tracked through up to 10 holograms this way, and a mean velocity was calculated from each time step (see Sect. 4.3). A visualization of the resulting particle property and particle track information can be seen for a sample measurement in Section S6 of the Supplement.

Calibration glass beads were used to conduct reference measurements of particle size and fall velocity for the particle tracking setup. "Dry Soda Lime Glass Microspheres" fabricated by Duke Standards (Fremont, CA, USA), the diameter of which was given by the manufacturer to be 29.5 ± 1.0 µm, were recorded while passing through the sample volume. The observed particle sizes, shown in Fig. 3a, showed that a sizing correction had to be applied to the determined particle sizes, which is common for holographic particle imaging (Lu et al., 2012). The particle size given by the manufacturer was confirmed by measuring the beads under a microscope, as well as by applying the sizing method using a sign-matched filter proposed by Lu et al. (2012) to the recorded holograms. Thus, all particle sizes determined using the approach described in Sect. 3.1.1 were corrected by subtracting a bias of 3 µm. The velocities and corrected diameters determined for 245 calibration beads are shown in Fig. 3b. The velocity calculated for spheres with a given diameter using Eq. (7) is plotted in black, with the uncertainty from density and size deviations ($\Delta\rho_g = \pm\ 100$ kg m^{-3}, $\Delta D = 2.5$ µm) as gray shading. The measured values are found in the vicinity of the theoretical curve, thus confirming the validity of the method.

3.1.3 Fall streak analysis

In a validation experiment, the velocities measured with particle tracking were compared with measurements obtained with a different, independent method. This approach used prolonged camera exposure to obtain a continuous recording of the moving ice particles' positions over an extended period of time. A fall streak effect with length s_{str} was created in the recorded images for each falling crystal (see Fig. 11a). The projection of the crystal's mean velocity onto the focal plane was then calculated via $v_{fall} = s_{str}/T_{exp}$, with the exposure time T_{exp}. The inherent size of the ice crystals, which was in the order of 1% of s_{str}, and thus negligible, was ignored in the streak length analysis. The vertical extent of each image was 24 mm. Combined with a camera exposure time of $T_{exp} = 85$ ms, the full length of fall streaks from crystals falling at up to 140 mm/s could be captured in each recording. As the contrast between the bright streaks created by falling crystals and the dark background was strong, it was possible to use a thresholding method for the automation of streak length measurements, yielding a velocity distribution for each recording. More detailed elaborations on the automated detection of objects in images using thresholding and other techniques are given in Sect. 3.2 and the Supplement.

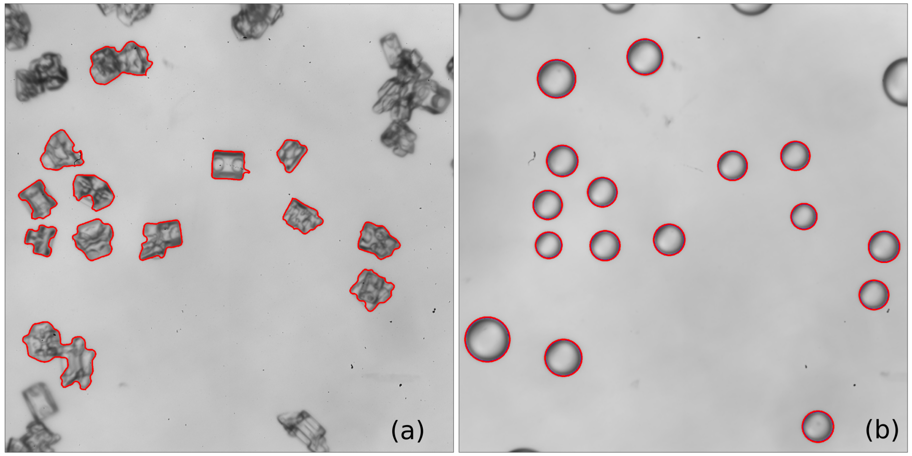

Figure 4. Sample images of ice crystals collected on a microscope slide before and after melting. The automatically detected contours (from k-means clustering segmentation (Pedregosa et al., 2011) in the crystal image and from Hough circle detection (Hough and Paul, 1962) in the droplet image) are added in red. Contours which intersect the image frame borders are discarded.

3.1.4 Evaluation of residual turbulence

Various steps have been taken in order to suppress any source of turbulence in the fall section, because a calm environment is required to obtain meaningful and unbiased results for the conducted fall speed measurements. Thermal insulation of the sample volume from the light sources required for fall speed measurements and air-tight sealing of the fall section relative to the surrounding cold room were ensured. Further, an air flow from the cooling unit of the ICC directly past the measurement section was created during the experimental process. This ventilation ensured that the fall section containing the measurement region is the coldest area of the cloud chamber volume, creating a statically stable region within the velocimetry sample volume to inhibit any turbulence potentially disturbing the crystals' falling motion. To verify that the remaining turbulence in the fall section is negligible, test experiments were conducted in which the droplet motion within the sample volume was recorded by a camera. The recorded video was then analyzed and, using tracking of individual droplets, the remaining drift velocity in the improved setup were estimated. The velocity of the weak random turbulent motion of droplets was estimated to be around $5\ \mathrm{mm\ s^{-1}}$.

3.2 Ice crystal mass

In order to relate the mass of individual ice crystals to a representative particle size, a microscopic imaging method was used. The crystals moving through the fall section (see bottom region in Fig. 1) were collected underneath the chamber on a glass slide treated with a hydrophobic silane. The glass slide was then extracted from the cloud chamber and its surface was covered with a millimeter-thick layer of oil to prevent sublimation of ice. Next, the coated slide was viewed and scanned under the magnification of a microscope, yielding images of several crystals in each picture.

Binarization method	$\overline{\lvert\Delta D_{sec}\rvert}$	$\overline{\lvert\Delta D_{ae}\rvert}$
Global Threshold	1.4 µm	1.2 µm
Adaptive Threshold	1.2 µm	1.7 µm
k-means clustering	1.1 µm	1.1 µm
Canny Edge Detection	1.5 µm	2.0 µm

Table 1. Mean error of ice crystal sizing relative to operator-labeled image for different binarization methods in a sample image. $\overline{|\Delta D_{sec}|}$ for diameter of smallest enclosing circle, $\overline{|\Delta D_{ae}|}$ for area equivalent diameter.

This method does not allow for a direct matching between individual mass and velocity data points. During each experiment, the set of crystals recorded on the microscope slide is the same set of crystals observed in the fall measurements, but connecting a single fall track to a crystal on the slide would require an extrapolation of the observed fall trajectory to predict the landing position on the slide. This extrapolation cannot be calculated with a sufficiently low level of uncertainty, thus the relationships between mass and fall velocity are only created in an ensemble approach.

To deduce size information from these microscope images, we have developed an automated image processing software which utilizes various object detection approaches to accurately trace the crystal edge contours. In addition to global and local grayscale thresholding, Canny edge detection (Canny, 1986) and k-means clustering (Pedregosa et al., 2011) were used to create several binarized representations of each image. From these binary images, the contour tracing approach developed by Suzuki and Abe (1985) was used to create object contours from which characteristic size parameters were obtained. A more thorough elaboration on the segmentation and contour tracing methods can be found in the Supplement.

The accuracy of the particle sizes obtained from the different binarization methods (see Table 1) was evaluated by creating a reference sizing and determining the deviation between particle sizes obtained from the binarized particle representations and the reference sizing. For this, the crystal edges in a sample image have been traced in zoomed-in views of the crystals by an operator. To compare the particle sizes obtained by these reference contours, two size parameters were evaluated: the diameter of the smallest enclosing circle around a contour, D_{sec}, and the area-equivalent diameter, D_{ae}. The sizing errors of each segmentation method with respect to these parameters were determined by applying them on a sample image containing 12 single crystals (Table 1). Obviously, the sizing error introduced by all methods was smaller than 2 µm, whereas the machine learning-based k-means clustering method provided the best agreement to the shapes determined by the operator. Similar results were observed for other images, with k-means yielding the most accurate results in most cases.

After completion of the crystal image acquisition, the microscope slide was exposed to a heating lamp, which let the ice crystals melt within a few minutes. Subsequently, a second image containing the resulting melted drops was recorded and the droplets' diameters were determined using the circle Hough Transform (CHT) algorithm (Hough and Paul, 1962). Due to the hydrophobic characteristics of the glass surface and the low density of the oil used for coating, the drops formed this way have an approximately spherical shape, allowing for a simple calculation of the water mass contained in each individual ice crystal (Fig. 4b).

Special caution had to be exerted when interpreting drop image data, as the coagulation of multiple melting crystals into a single drop had been observed on several occasions. To prevent this effect from creating a bias in measurement data, affected mass-dimension pairs were removed after the automated image analysis through manual post-processing.

3.3 Particle size

As summarized by Wu and McFarquhar (2016), the size of ice crystals is described in a variety of different ways throughout the literature, and an appropriate interpretation is required when comparing size data from different sources. For analysis of the microscope images in this study with the goal of determining particle size, the diameter D_{sec} of the smallest enclosing circle around the detected crystal contour, and the area equivalent diameter D_{ae} were determined and used for deriving the $m(D)$ relationships. These length scales were chosen because it is possible and straight forward to determine them without any assumptions regarding the third dimension from the image data at hand. For the velocity measurements, the recorded particle images in the described holography setup are 2D projections of the crystals during their fall. The length of the major axis of an ellipse fitted to the particle's contour, D_{maj}, was used as the parameter representing particle size~~.~~, as this is a common approach for holographic particle measurements. The hydrodynamic diameter D_{hyd} is determined in Section 4 as a length scale that meaningfully describes the fall behavior of the investigated objects.

4 Results and discussion

Ice crystal properties were determined by analyzing the images and holograms obtained in a total of 18 experiments conducted in the ICC. In order to produce ice crystals of different habits, the conditions within the chamber during particle growth were varied between experimental runs. The chamber temperature was set to values between -8 and $-16\,^{\circ}\mathrm{C}$ and monitored continuously with a thermocouple sensor. Additionally, ice crystal growth is determined by the available water vapor inside of the ICC, which could be influenced indirectly by adjusting the rate and duration of droplet supply into the chamber volume. Since the initial freezing event is triggered by the very low temperatures below $-80\ ^{\circ}\mathrm{C}$ in the vicinity of the cold finger, the shapes observed in the sampling regions are not strictly exclusively a product of the conditions in the chamber. In a comparison experiment, the cold finger was deactivated and droplets containing INP were sprayed into the chamber instead. Investigations using the same methods that were used for the cold finger experiments yielded a similar distribution of crystal habits and irregular crystal shapes similar to the ones observed in the cold finger experiments. While an impact of the freezing mechanism on the microphysical properties of the observed crystals can not be fully ruled out, no negative impact on the applicability of this work's results to atmospheric processes has been observed.

4.1 Cloud characterization

In order to characterize the thermodynamic conditions of the ICC during typical measurement conditions, the liquid water content (LWC) of the chamber air was determined. For this, the dew point temperature $T_{d,dry}$ of chamber air was determined before an experiment cycle (dry conditions) by sampling chamber air isokinetically into a dew point hygrometer (MBW Calibration Ltd., Wettingen, Switzerland, DP3-D/SH) placed outside the cold room. Afterwards, a cloud of liquid droplets was generated as usual for an experimental run, and chamber air containing droplets was sampled and lead to the hygrometer. In order to evaporate the droplets within the sampled air, the walls of the tube from the chamber towards the hygrometer were heated, inducing an increase in temperature within the tube itself. As relative humidity was thus reduced below saturation, the droplets flowing through the tube evaporated before the sampled air mass reached the dew point hygrometer. The increase in absolute humidity Δq within the chamber between dry and cloud-filled conditions is given in Table 2, and it was determined from the measured dew point temperatures and saturation vapor pressures:

$$LWC = \Delta q = \frac{e_{s,cloud}}{R_v T_{d,cloud}} - \frac{e_{s,dry}}{R_v T_{d,dry}}, \tag{8}$$

where $e_{s,cloud}$, $e_{s,dry}$, T_{cloud} and T_{dry} are the saturation vapor pressures and temperatures during cloud and dry conditions and $R_v = 461.4$ J kg^{-1} K^{-1} is the individual gas constant for water vapor. The saturation vapor pressures were determined using the Magnus approximation to the Clausius-Clapeyron equation (Alduchov and Eskridge, 1996). The increase in dew point temperature of 7.5 K (see Tab. 2) corresponds to a LWC of 1.61±0.22 gm^{-3} within the ICC during typical cloud conditions before nucleation was triggered. This value is similar to observations within typical atmospheric cumulus clouds (Bower and Choularton, 1988). In a separate experiment using the holography setup described in Sect. 4.3, the droplet size distribution in the fully-formed cloud was determined to have its mode at about 10 µm. When combining the determined mean droplet size and LWC, the number concentration of droplets within the ICC cloud can be calculated to be approximately 2500 cm^{-3}.

4.2 Mass measurements

A total of 1207 pairs of ice crystals and melted droplets were obtained from microscope imaging and the melting technique, with crystal area equivalent diameters between 15 and 145 µm. The majority of ice crystals ($\approx 68\%$) showed irregular crystal growth, with complex angular shapes being more frequent than rounded shapes. For pristine crystals, a dependence of growth

	T_d [K]	e_s [hPa]	q [gm^{-3}]
Dry conditions	262.0±0.5	2.66±0.11	2.20±0.08
Cloud conditions	269.5±0.5	4.73±0.18	3.81±0.14

Table 2. Dew point temperature and deduced humidity measures for liquid water content measurements. The increase in dew point temperature was caused by the evaporation of droplets on their way from the ICC to the dew point hygrometer. e_s was calculated from the Magnus approximation to the Clausius-Clapeyron equation, q from Eq. (8).

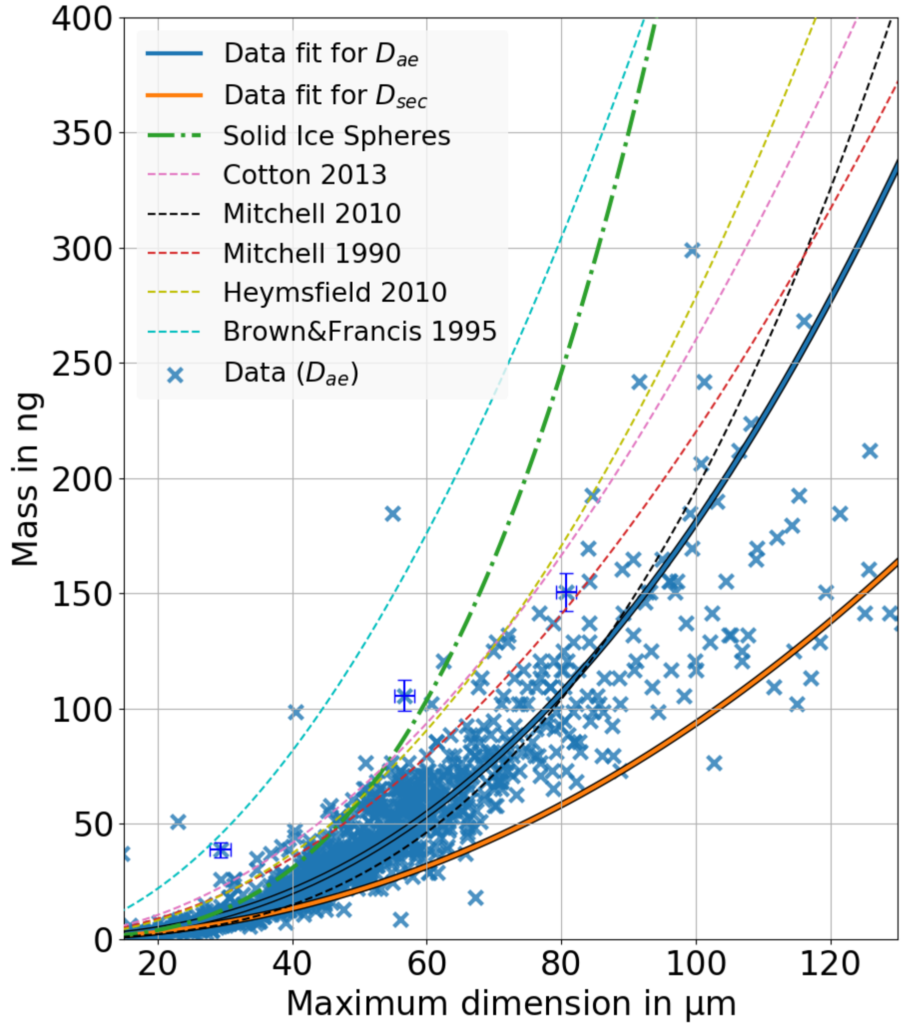

Figure 5. Ice crystal mass as a function of maximum dimension from the present ICC experiments (N = 1207, D_{ae} in blue, best fit as solid blue line; D_{sec} best fit as orange solid line). Parameterizations from literature are plotted by dashed lines. The green dash-dotted line shows the mass of a spherical object with density $\rho_{ice} = 0.9184\ \mathrm{kg\ m^{-3}}$

.

habit on the thermodynamic conditions was observed. The most frequent pristine shape was columns ($\approx 20\%$), followed by aggregates of pristine and irregular crystals ($\approx 7\%$), and dendrites ($\approx 4\%$). Capped columns, bullet rosettes, and plate crystals were all observed with a fraction of 1% or less.

Figure 5 shows the mass of ice crystals as a function of their size. The blue crosses are data points of the area-equivalent diameter D_{ae} of crystals obtained from the experiments described in Sect. 3~~, with the~~ . The blue solid line ~~representing~~ represents the best power law fit to this data, given by $m = 0.4972 D^{2.36}$, with D given by the area equivalent diameter of the crystals, D_{ae}. The solid orange line represents the best fit to data obtained from the experiments in the present study if crystal size is interpreted as the diameter of the smallest enclosing circle around the crystal contour determined by automated object detection (D_{sec})~~.~~, with $m = 0.0397D^{2.13}$.

Also added are power law relationships ~~of Cotton et al. (2013), Mitchell et al. (2010), Mitchell et al. (1990), Heymsfield et al. (2010) and Brown and Francis (1995) for comparison.~~ from several other studies for comparison. For the study in Mitchell et al. (1990), ice crystals of all habits with varying degrees of riming and a maximum dimension between 200 and 7700 µm were collected in orographic winter storms. Their masses were also determined from melting and measuring the remaining water drops' sizes on a surface. Brown and Francis (1995) determined IWC and particle size distributions (PSD) of ice clouds containing mostly ice crystals with sizes between 200 and 800 µm from a combination of instruments during an airborne measurement campaign, and used them to formulate an m(D) power law relationship for quasi-spherical irregular ice crystals. Heymsfield et al. (2010) combined the results of 6 field measurement campaigns by following a similar approach based on IWC and PSD, which yielded a parameterization based on ice crystals of all habits and degrees of riming in a size range between 100 and 2000 µm in median mass diameter. Cotton et al. (2013) analyzed the results of a different aircraft campaign with a similar method of relating IWC and PSD for clouds containing mostly featureless ice crystals with a maximum diameter between 20 and 800 µm. The parameterization from Mitchell et al. (2010), which is proposed for ice crystals smaller than 240 µm, is based on a combination of satellite-retrieved PSD and in-situ measurements of IWC.

It can be seen that the ice particle masses predicted by most of the parameterizations from the literature are higher than those observed in the present study. An exception is the relation given by Mitchell et al. (2010), which is the only relationship that is also determined with a focus on small crystals rather than an extrapolation from measurements of larger crystals. It shows good agreement with our parameterizations up to around 100 µm.

4.3 Sedimentation velocity measurements

In Fig. 6, the measurements of ice crystal sedimentation velocity and size are shown for eight experiments conducted in the ICC. Following the varying thermodynamical conditions, different distributions of observed crystal habits were present during each experiment. As expected, a large spread was found in the observed fall velocities, which ranged from a few mm s^{-1} to 120 mm s^{-1}.

The hydrodynamic diameter of the falling crystals, which serves as a good descriptor of the hydrodynamic properties of a falling object, can be calculated from Eq. (7):

$$D_{hyd} = \frac{g}{3\pi\eta}\frac{m}{v}. \quad (9)$$

If ~~$D_{hyd} < D_{max}$~~$D_{hyd} \leq D_{maj}$, the observed falling object has a ratio between m and v that is smaller than that of a sphere of diameter ~~D_{max}~~D_{maj}. In Fig. 7, D_{hyd} is shown as a function of D_{maj} for all crystals observed in the fall track experiments. ~~$D_{hyd}/D_{maj} < 1$ for~~ Most crystals with $D_{maj} <$~~, increasing with D_{maj} and crossing the value of 1 ($D_{hyd} = D_{maj}$) at around $D_{maj} =$. Crystal habit and size show good correlation, as most crystals with $D_{maj} <$~~70 µm have grown with a columnar or irregular habit, and larger crystals were mostly dendritic or aggregated. Nevertheless, no distinct dependence of the ratio

D_{hyd}/D_{maj} on habit can be observed as seen in Fig. 8). The difference between the mean ratios D_{hyd}/D_{maj} observed in each of the other habits is smaller than the standard deviation of D_{hyd}/D_{maj} within each habit class (represented by error bars). The small mean ratio for capped columns is an artifact of the small sample size of this particular habit.

$D_{hyd}/D_{maj} < 1$ for crystals with $D_{maj} <$100 µm, increasing with D_{maj} and crossing the value of 1 ($D_{hyd} = D_{maj}$) at around $D_{maj} =$ 100 µm. To understand this behavior, it has to be repeated that m in Eq. 9 is determined from the parameterization given in Section 4.2. Firstly, the $m(D)$ parameterization was determined for the area-equivalent diameter of a crystal contour D_{ae} and is thus not applicable strictly without error when considering D_{maj} in this context. Further, the mass parameterization is most strongly determined by ice particles with sizes around 60 µm and, as evident from Fig. 5, mostly overestimates the mass of crystals with $D >$ 100 µm. This overestimation of m also leads to an overestimation of D_{hyd} for those larger crystals. It is not expected that $D_{hyd} > D_{maj}$ would be observed for any individual measurement.

The relationship between D_{hyd} and ~~D_{max}~~ D_{maj} for crystals of all observed ~~sizes and shapes~~ shapes with $D_{maj} <$ 90 µm follows the power law ~~$D_{hyd} = 0.039 D_{max}^{1.69}$.~~ $D_{hyd} = 0.039 D_{maj}^{1.69}$. For larger D_{maj}, a relationship convering towards $D_{hyd} = D_{maj}$ would be expected.

Additionally, a separate analysis of columnar crystals has been conducted to complement the investigation where all crystals of different habits were combined. Columns were chosen due to their abundance in the experiments (over 20% of all observed crystals) and their symmetric shape, which allows for an appropriate estimation of their projected area during fall. The Best numbers X (see Eq. (5)) of the observed columns ranges between 10^{-1} and 10 (see Fig. 9), with Reynolds numbers (see Eq. (4)) between 0.05 and 0.5. The observed fall behavior is thus not strictly in the Stokes regime (where Re would be « 1), with turbulence having a minor impact on the observed fall velocity. This impact increases with increasing D_{maj}. Furthermore, the mean aspect ratio (AR) of columns investigated in this work was 0.49. The data fit (orange line, with its uncertainty as gray shading) is enveloped by both curves from Jayaweera and Cottis (1969), who determined X and Re for metal cylinders with two different aspect ratios falling in motor oil. The power law relationship suggested by Bürgesser et al. (2016) generally predicts significantly higher Best numbers than we observed for a given Reynolds number.

For low Reynolds numbers ($Re \ll 1$), both theoretical models and experimental studies suggest that the orientations of falling columns are randomly distributed (Westbrook, 2007; Bürgesser et al., 2016). The same behavior can be seen in the distribution of orientations of the falling columnar crystals in our study, which do not show any preferred alignment of crystals to the fall direction (see Fig. 10).

4.4 Fall streak measurements

The velocity range measured using particle streaks during the validation experiment was similar to the range prevalent in the holographic measurements, with a mode in the velocity distribution around $v_{sed} = 40$ mm/s for both techniques. To further characterize the fall behavior of crystals in the fall section, the spatial distribution of fall streak center points detected in each part of the sample volume during the validation experiment is shown in Fig. 11b. Streaks could be observed throughout the entire field of view of the camera. Nevertheless, the image edges were slightly less populated, which is a result of the filtering of incomplete fall streaks extending outside of the field of view. Figure 11c shows the evolution of the mean particle fall velocity over time for the fall streak experiment. The dashed lines show the moving average of the fall speeds' standard deviation in each image. The highest mean velocities were detected in the early phase of the experiment, as the fastest crystals arrived in the sample volume first. After around 10 s, the velocity reached a steady level. In this phase, a mix of crystals with high and low fall velocities was present in each layer of the chamber due to the constant resupply of newly formed crystals. From this point on, a slow decline of the mean fall velocity was observed because the crystals remaining in the section slowly sedimented out.

Figure 12 shows the distribution of velocities from a set of streak measurements (top panel) and the size distribution of ice crystals measured under the microscope afterwards. A similar general shape can be observed, with a steep increase from low values to a mode in an intermediate region (15 mm/s for w, 30 µm for D_{ae}) and a longer tail towards higher values. The bottom panel shows the histogram of sedimentation velocities calculated from D_{ae} following Stokes theory (Eq. (7)) for each crystal, using the $m(D)$ power law determined in subsection 4.2 for mass calculation ($a = 0.4972$, $b = 2.36$). While the general shapes of the distributions are roughly similar, the mode of observed velocities (top panel) is found at slightly lower velocity values than the one in the distribution predicted by Stokes theory. This implies that the observed crystals are subjected to a stronger drag force than a spherical object with diameter D_{ae} falling in the Stokes regime.

5 Conclusions

During experiments conducted in the ice cloud chamber of the Mainz vertical wind tunnel laboratory, in-focus images of small ice crystals with sizes between 25 and 220 µm during their sedimentation in a calm environment from reconstructed holograms were produced. From these images, sedimentation velocities of over 3500 particles have been obtained by particle tracking. After classifying the crystals based on their habits, a relationship between hydrodynamic and maximum diameter was calculated. A separate analysis was conducted for columnar crystals, which were the most frequently observed crystals of regular shape. The relationship between Best and Reynolds numbers that was determined for columnar crystals agreed well with the parameterization from Jayaweera and Cottis (1969). The mass of 1207 crystals was determined by collecting the crystals on a glass slide and measuring their size before and after melting. A parameterization relating particle mass and maximum dimension was calculated, which describes the properties of ice crystals in the investigated size range more accurately than similar relationships found in the literature.

The analysis methods used for determining the particle properties were almost entirely automated requiring minimal operator interaction, owing to the capabilities of modern computer vision and machine learning algorithms. The accuracy of data obtained through these automated processes was validated through comparison to operator-labeled samples. The automation accelerated the acquisition and analysis of new data.

Sensitivity studies on the effect of the proposed mass parameterizations on atmospheric models should be conducted in order to evaluate their impact on the formation and persistence of clouds containing small ice crystals, because the processes involved include too many complex feedback mechanisms to allow for an immediate, general conclusion. Conducting such sensitivity studies is suggested here, as our literature search did not reveal any assessments investigating the subject.

The Supplement related to this article is available online at [insert supplement URL].

Code and data availability. Software code and experimental data are freely available upon request to the contact author.

Author contributions. MW, SKM, JF, and SB designed research and instrumentation; MW performed research and evaluated data; MW, MS and SB drafted the manuscript.

Competing interests. The authors declare that they have no conflict of interest.

Acknowledgements. This work was supported by the Max Planck Graduate Center and internal funds from the Max Planck Institute for Chemistry.

References

Alduchov, O. A. and Eskridge, R. E.: Improved Magnus form approximation of saturation vapor pressure, https://doi.org/10.1175/1520-0450(1996)035<0601:IMFAOS>2.0.CO;2, 1996.

Baumgardner, D., Abel, S. J., Axisa, D., Cotton, R., Crosier, J., Field, P., Gurganus, C., Heymsfield, A. J., Korolev, A., Krämer, M., Lawson, P., McFarquhar, G., Ulanowski, Z., and Um, J.: Cloud Ice Properties: In Situ Measurement Challenges, Meteorological Monographs, 58, 9.1–9.23, https://doi.org/10.1175/AMSMONOGRAPHS-D-16-0011.1, http://journals.ametsoc.org/doi/10.1175/AMSMONOGRAPHS-D-16-0011.1, 2017.

Borrmann, S., Jaenicke, R., and Neumann, P.: On spatial distributions and inter-droplet distances measured in stratus clouds with in-line holography, Atmospheric Research, 29, 229–245, https://doi.org/10.1016/0169-8095(93)90005-9, 1993.

Bower, K. N. and Choularton, T. W.: The effects of entrainment on the growth of droplets in continental cumulus clouds, Quarterly Journal of the Royal Meteorological Society, 114, 1411–1434, https://doi.org/10.1002/qj.49711448404, 1988.

Breiman, L., Friedman, J. H., Olshen, R. A., and Stone, C. J.: Classification and regression trees, CRC Press, https://doi.org/10.1201/9781315139470, 2017.

Brown, P. R. and Francis, P. N.: Improved Measurements of the Ice Water Content in Cirrus Using a Total-Water Probe, Journal of Atmospheric and Oceanic Technology, 12, 410–414, https://doi.org/10.1175/1520-0426(1995)012<0410:IMOTIW>2.0.CO;2, 1995.

Bürgesser, R. E., Ávila, E. E., and Castellano, N. E.: Laboratory measurements of sedimentation velocity of columnar ice crystals, Quarterly Journal of the Royal Meteorological Society, 142, 1713–1720, https://doi.org/10.1002/qj.2766, 2016.

Canny, J.: A Computational Approach to Edge Detection, IEEE Transactions on Pattern Analysis and Machine Intelligence, https://doi.org/10.1109/TPAMI.1986.4767851, 1986.

Cotton, R. J., Field, P. R., Ulanowski, Z., Kaye, P. H., Hirst, E., Greenaway, R. S., Crawford, I., Crosier, J., and Dorsey, J.: The effective density of small ice particles obtained from in situ aircraft observations of mid-latitude cirrus, Quarterly Journal of the Royal Meteorological Society, 139, 1923–1934, https://doi.org/10.1002/qj.2058, http://doi.wiley.com/10.1002/qj.2058, 2013.

Davies, C. N.: Definitive equations for the fluid resistance of spheres, Proceedings of the Physical Society, 57, 259–270, https://doi.org/10.1088/0959-5309/57/4/301, 1945.

Fugal, J. P., Shaw, R. A., Saw, E. W., and Sergeyev, A. V.: Airborne digital holographic system for cloud particle measurements, Applied Optics, 43, 5987, https://doi.org/10.1364/ao.43.005987, 2004.

Fugal, J. P., Schulz, T. J., and Shaw, R. A.: Practical methods for automated reconstruction and characterization of particles in digital in-line holograms, Measurement Science and Technology, 20, https://doi.org/10.1088/0957-0233/20/7/075501, 2009.

Heymsfield, A. J., Van Zadelhoff, G.-J., Donovan, D. P., Fabry, F., Hogan, R. J., and Illingworth, a. J.: Refinements to ice particle mass dimensional and terminal velocity relationships for ice clouds, Part II: Evaluation and parameterizations of ensemble ice particle sedimentation velocities, Journal of the Atmospheric Sciences, 64, 1068–1088, https://doi.org/10.1175/JAS3900.1, http://dx.doi.org/10.1175/JAS3900.1, 2007.

Heymsfield, A. J., Schmitt, C. G., Bansemer, A., and Twohy, C. H.: Improved Representation of Ice Particle Masses Based on Observations in Natural Clouds, Journal of the Atmospheric Sciences, 67, 3303–3318, https://doi.org/10.1175/2010JAS3507.1, http://journals.ametsoc.org/doi/abs/10.1175/2010JAS3507.1, 2010.

Hough, V. and Paul, C.: U.S. Patent 3,069,654: Method and means for recognizing complex patterns, 1962.

Hubbard, J. B. and Douglas, J. F.: Hydrodynamic friction of arbitrarily shaped Brownian particles, Physical Review E, 47, https://doi.org/10.1103/PhysRevE.47.R2983, 1993.

Jayaweera, K. O. L. F. and Cottis, R. E.: Fall velocities of plate-like and columnar ice crystals, Quarterly Journal of the Royal Meteorological Society, 95, 703–709, https://doi.org/10.1002/qj.49709540604, 1969.

Locatelli, J. D. and Hobbs, P. V.: Fall speeds and masses of solid precipitation particles, Journal of Geophysical Research, 79, 2185, https://doi.org/10.1029/JC079i015p02185, 1974.

Lu, J., Shaw, R. a., and Yang, W.: Improved particle size estimation in digital holography via sign matched filtering, Optics Express, 20, 12 666, https://doi.org/10.1364/OE.20.012666, 2012.

Mitchell, D. L.: Use of Mass- and Area-Dimensional Power Laws for Determining Precipitation Particle Terminal Velocities, Journal of the Atmospheric Sciences, 53, 1710–1723, https://doi.org/10.1175/1520-0469(1996)053<1710:UOMAAD>2.0.CO;2, 1996.

Mitchell, D. L., Zhang, R., and Pitter, R. L.: Mass-Dimensional Relationships for Ice Particles and the Influence of Riming on Snowfall Rates, Journal of Applied Meteorology, 29, 153–163, 1990.

Mitchell, D. L., D'Entremont, R. P., and Lawson, R. P.: Inferring Cirrus Size Distributions through Satellite Remote Sensing and Microphysical Databases, Journal of the Atmospheric Sciences, 67, 1106–1125, https://doi.org/10.1175/2009JAS3150.1, 2010.

Molleker, S., Borrmann, S., Schlager, H., Luo, B., Frey, W., Klingebiel, M., Weigel, R., Ebert, M., and Mitev, V.: Microphysical properties of synoptic-scale polar stratospheric clouds : in situ measurements of unexpectedly large HNO 3 -containing particles in the Arctic vortex, Atmospheric Chemistry and Physics, 14, 10 785–10 801, https://doi.org/10.5194/acp-14-10785-2014, 2014.

Pedregosa, F., Michel, V., Grisel, O., Blondel, M., Prettenhofer, P., Weiss, R., Vanderplas, J., Cournapeau, D., Varoquaux, G., Gramfort, A., Thirion, B., Grisel, O., Dubourg, V., Passos, A., Brucher, M., Perrot, M., and Duchesnay, É.: Scikit-learn: Machine Learning in Python, Tech. rep., Parietal, INRIA Saclay, http://scikit-learn.sourceforge.net., 2011.

Raupach, S. M., Vössing, H. J., Curtius, J., and Borrmann, S.: Digital crossed-beam holography for insitu imaging of atmospheric ice particles, Journal of Optics A: Pure and Applied Optics, 8, 796–806, https://doi.org/10.1088/1464-4258/8/9/014, 2006.

Schlenczek, O.: Airborne and ground-based holographic measurement of hydrometeors in liquid-phase, mixed-phase and ice clouds, Ph.D. thesis, Johannes Gutenberg-Universität Mainz, 2018.

Silverman, B. A., Thompson, B. J., and Ward, J. H.: A Laser-Fog Disdrometer, https://doi.org/10.1175/1520-0450(1964)003<0792:alfd>2.0.co;2, 1964.

Suzuki, S. and Abe, K.: Topological Structural Analysis of Digitized Binary Images by Border Following, Computer Vision, Graphics and Image Processing, 30, 32–46, https://doi.org/10.1016/0734-189X(85)90016-7, https://ac.els-cdn.com/0734189X85900167/1-s2.0-0734189X85900167-main.pdf?{_}tid=daf865e6-5f8e-4ca6-a3f5-25ea77e44196{&}acdnat=1543244137{_}c90b0c3fe518c5131e275c9eb486934d, 1985.

Westbrook, C. D.: The fall speeds of sub-100um ice crystals, Quarterly Journal of the Royal Meteorological Society, 134, 1243–1251, https://doi.org/10.1002/qj, http://onlinelibrary.wiley.com/doi/10.1002/qj.71/abstract, 2007.

Wu, W. and McFarquhar, G. M.: On the impacts of different definitions of maximum dimension for nonspherical particles recorded by 2D imaging probes, Journal of Atmospheric and Oceanic Technology, 33, 1057–1072, https://doi.org/10.1175/JTECH-D-15-0177.1, 2016.

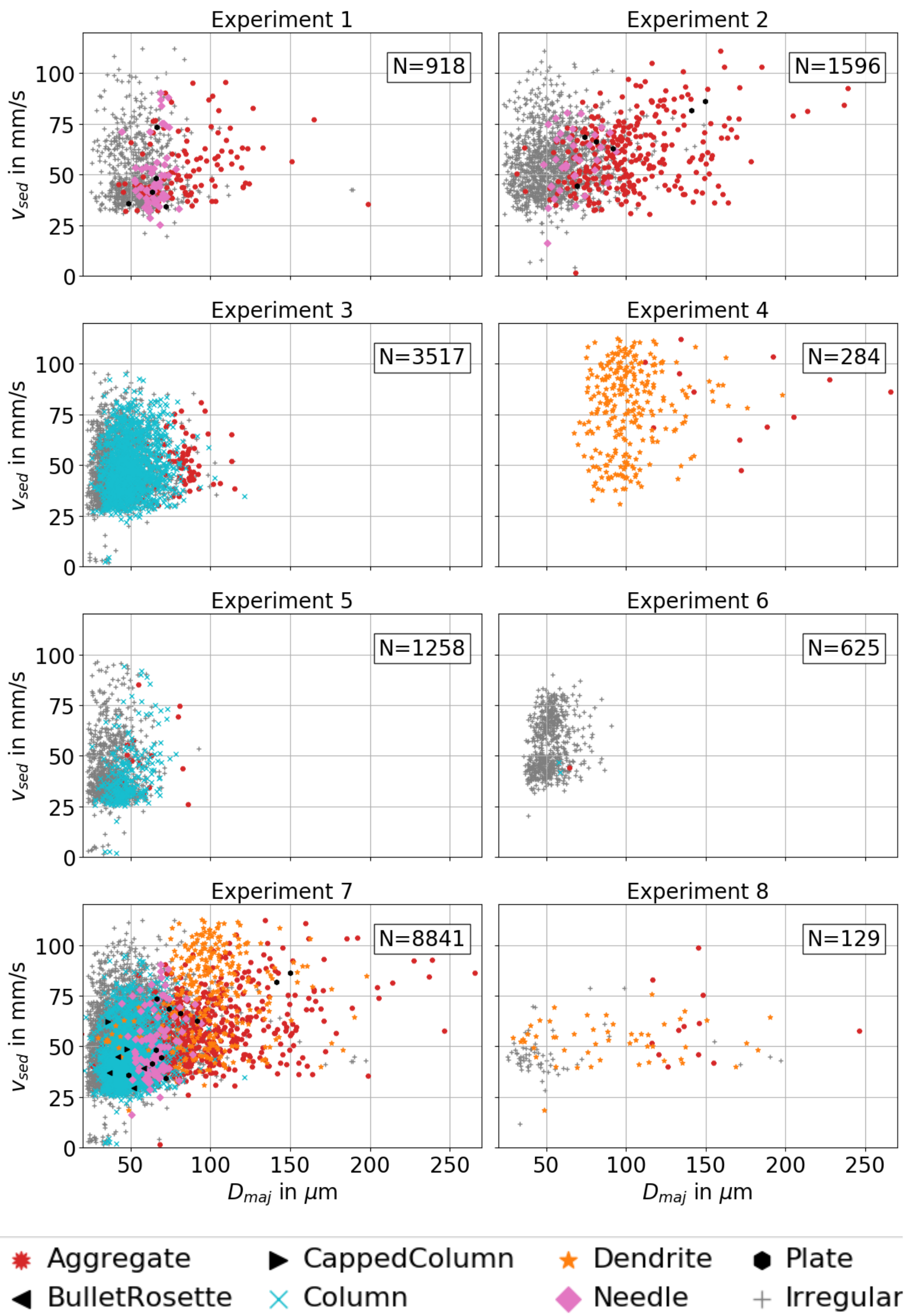

Figure 6. Sedimentation velocity (v_{sed}, in $\mathrm{mm/s}$) and size (D_{maj} in µm) measurements from holography particle tracking experiments (particle numbers in each experiment are annotated).

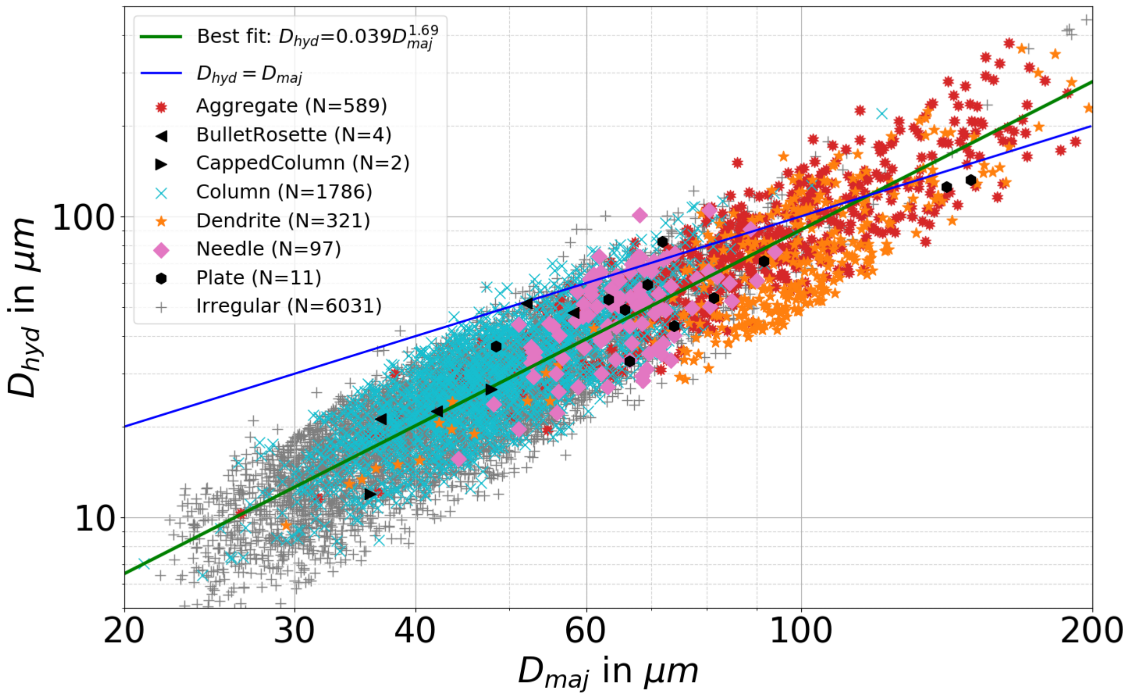

Figure 7. Relation between the hydrodynamic diameter D_{hyd} calculated using Eq. (7) and the measured ~~maximum dimension D_{max}~~ particle size D_{maj} of falling crystals. Different crystal habits (classified by the trained predictor) are marked as different symbols and colors. Power law fit as green line, ~~$D_{hyd}=0.039D_{maj}^{0.69}$~~$D_{hyd}=0.039D_{maj}^{1.69}$, with both D_{hyd} and D_{maj} in μm. The blue line represents ~~$D_{hyd}=D_{max}$~~$D_{hyd}=D_{maj}$.

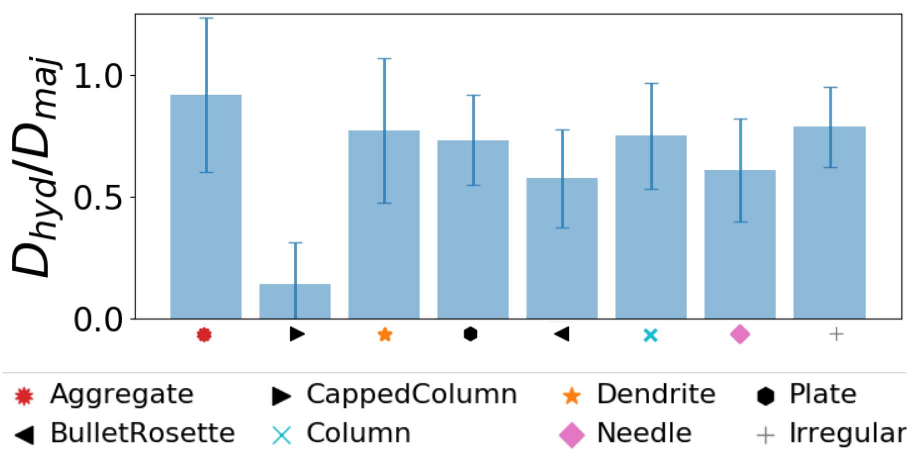

Figure 8. Mean value of D_{hyd}/D_{maj} for each crystal habit for data shown in Fig. 7.

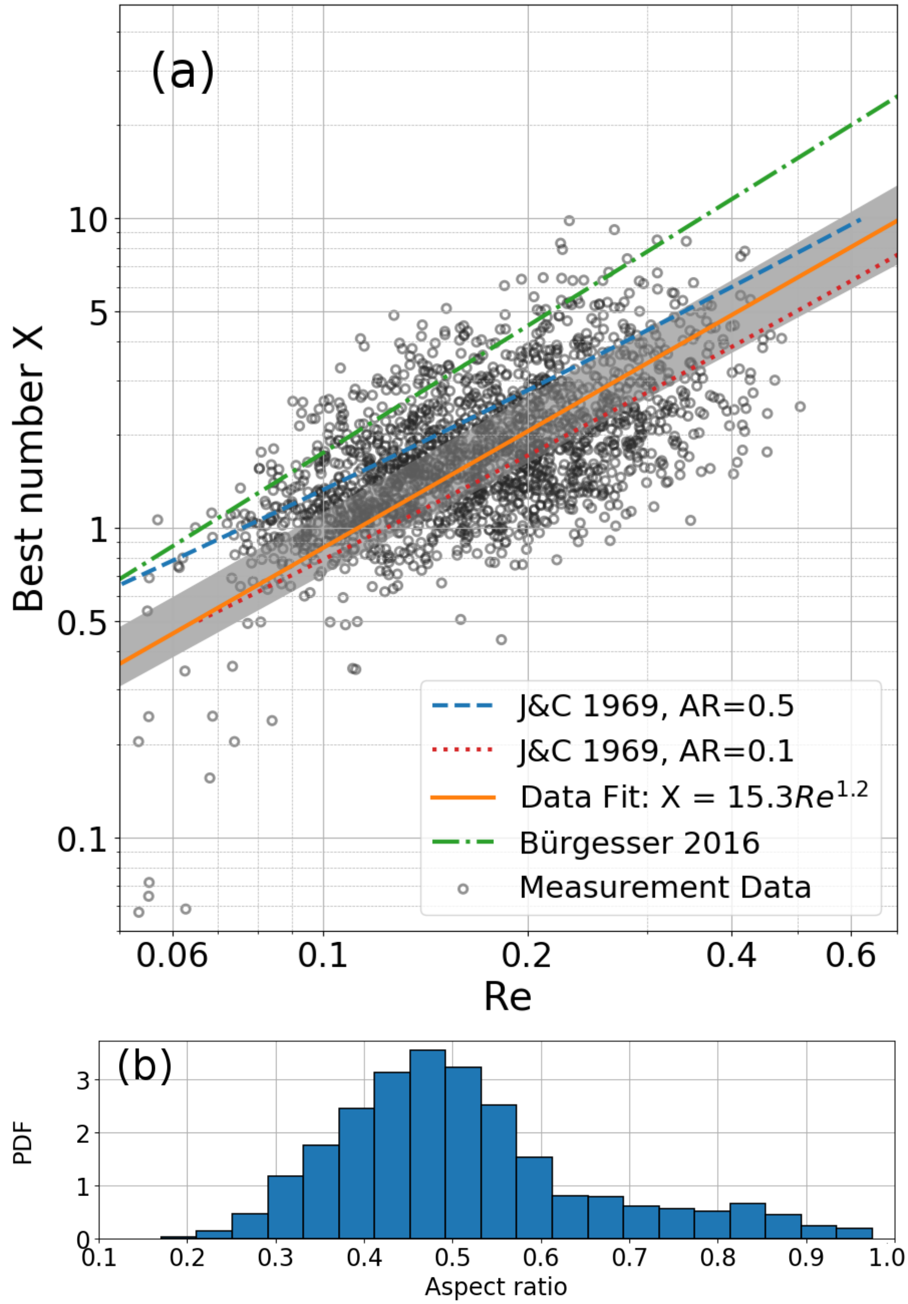

Figure 9. (a): Best number as function of Reynolds numbers for investigated falling columnar crystals, $N = 1844$. Data fit added in orange with error range as gray shading. Parameterization from Jayaweera and Cottis (1969) in magenta and orange, from Bürgesser et al. (2016) in green. **(b)**: Aspect ratio histogram of investigated columnar crystals, mean aspect ratio $\overline{AR} = 0.49$.

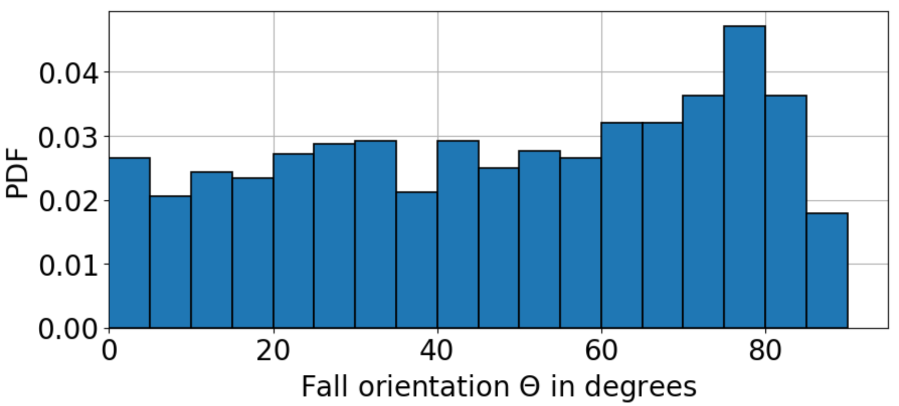

Figure 10. Histogram of the falling columnar crystals' orientation Θ, with 90° corresponding to a fall with the major axis normal to the falling direction. $N = 1844$.

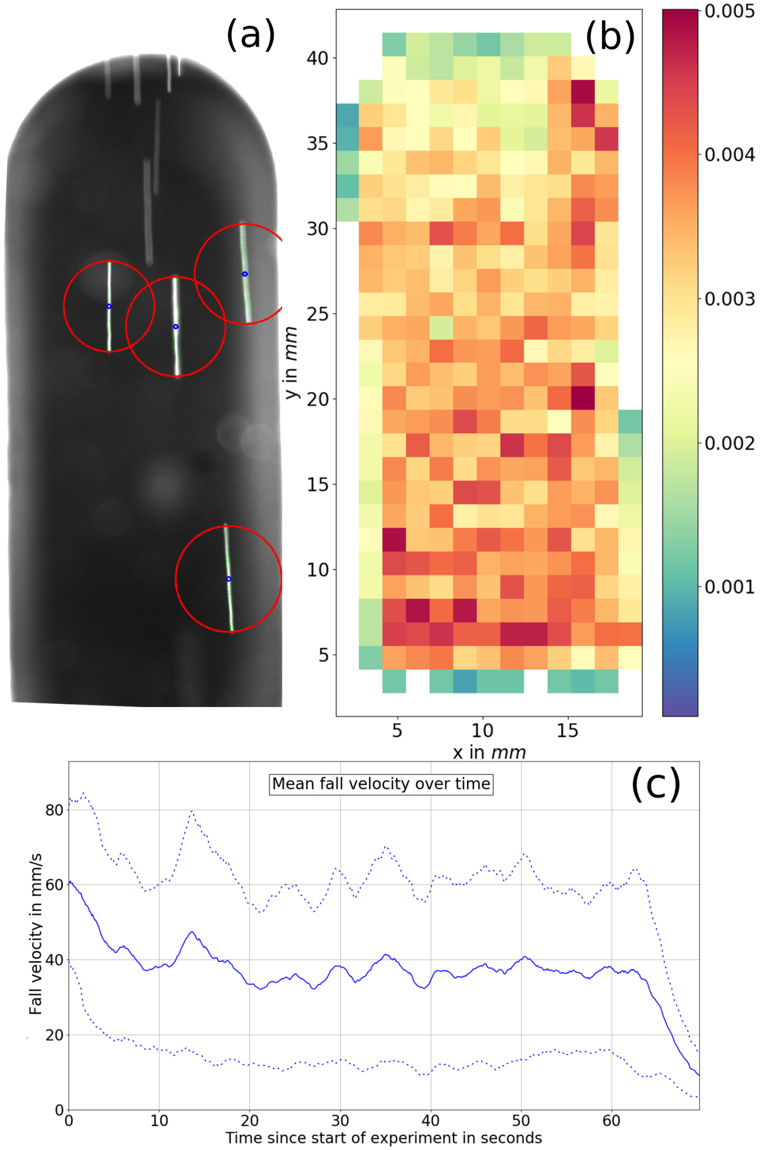

Figure 11. **(a)**: Example fall streak image. Detected streaks are circled in red, diameter is equal to the detected streak length. **(b)**: Relative occurrence of crystals in partial regions of the sample volume, number of streak center points observed in pixel region divided by number of streaks in the full image. Total number of streaks in experiment: $N = 24775$. **(c)**: Mean velocity of all falling objects in the sample volume over time. A moving average over 2 seconds was used to smooth the time series. The dashed lines show the moving average of the fall speeds' standard deviation in each image.

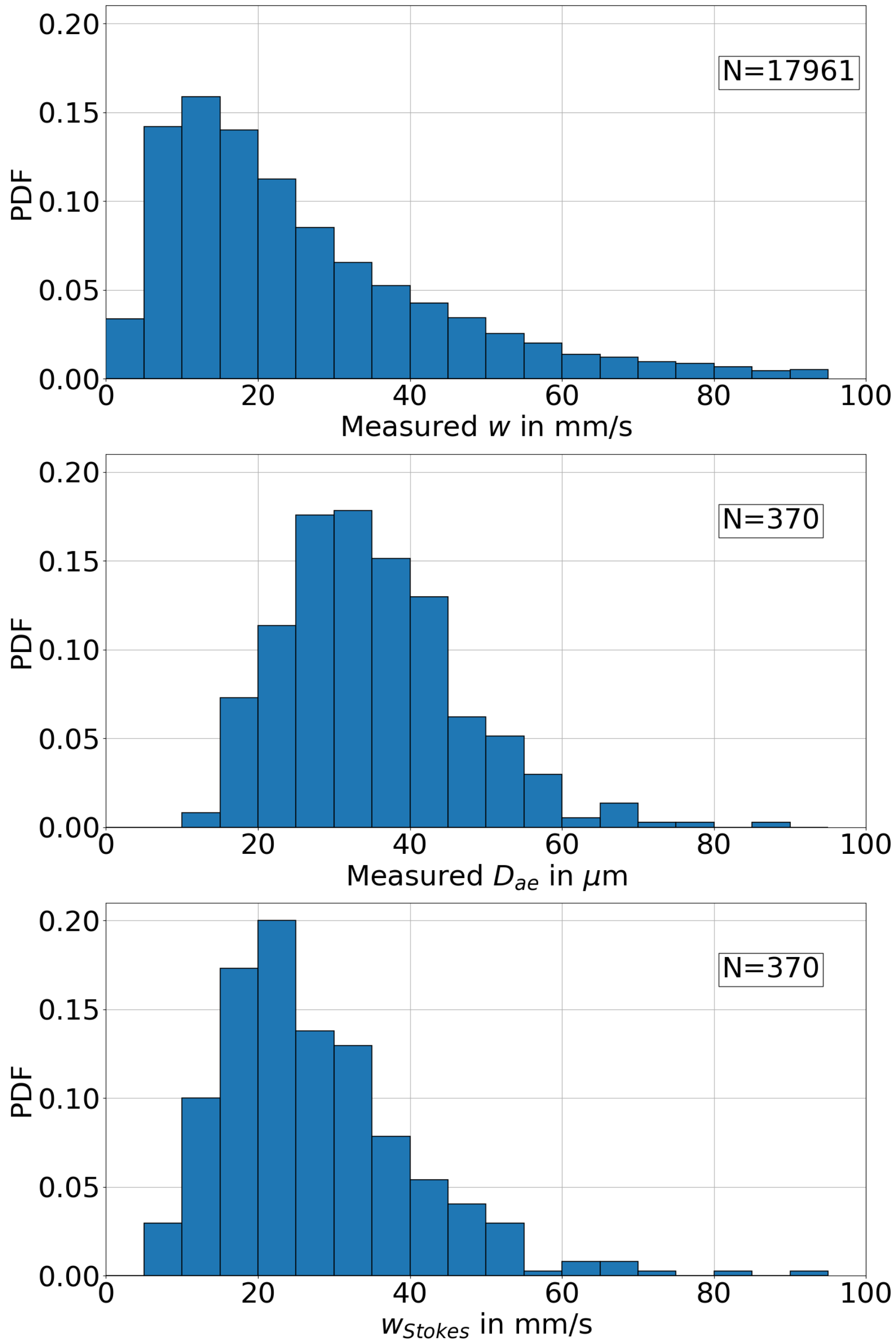

Figure 12. Distribution of different parameters for fall streak experiment. **(a)**: crystal fall velocities extracted from streak images. **(b)**: area-equivalent diameter (D_{ae}) from microscope images of collected crystals. **(c)**: fall velocity predicted from D_{ae} size distribution using Stokes theory (Eq. (7)).